NANO · MICRO small
www.small-journal.com

Creation of Single Vacancies in hBN with Electron Irradiation

Thuy An Bui, Gregor T. Leuthner, Jacob Madsen, Mohammad R. A. Monazam, Alexandru I. Chirita, Andreas Postl, Clemens Mangler, Jani Kotakoski, and Toma Susi**

Understanding electron irradiation effects is vital not only for reliable transmission electron microscopy characterization, but increasingly also for the controlled manipulation of 2D materials. The displacement cross sections of monolayer hexagonal boron nitride (hBN) are measured using aberration-corrected scanning transmission electron microscopy in near ultra-high vacuum at primary beam energies between 50 and 90 keV. Damage rates below 80 keV are up to three orders of magnitude lower than previously measured at edges under poorer residual vacuum conditions, where chemical etching appears to dominate. Notably, it is possible to create single vacancies in hBN using electron irradiation, with boron almost twice as likely as nitrogen to be ejected below 80 keV. Moreover, any damage at such low energies cannot be explained by elastic knock-on, even when accounting for the vibrations of the atoms. A theoretical description is developed to account for the lowering of the displacement threshold due to valence ionization resulting from inelastic scattering of probe electrons, modeled using charge-constrained density functional theory molecular dynamics. Although significant reductions are found depending on the constrained charge, quantitative predictions for realistic ionization states are currently not possible. Nonetheless, there is potential for defect-engineering of hBN at the level of single vacancies using electron irradiation.

1. Introduction

Transmission electron microscopy (TEM) is a powerful probe of the atomic structure of materials, and is particularly well suited to directly reveal any defects in the lattice of the specimen. The pioneering work of Crewe[1] marks the beginning of practical scanning transmission electron microscopy (STEM). From then on, the scanning probe mode was developed as a technique complementary to broad-beam illumination. Due to annular dark-field detection, yielding direct atomic-number contrast, STEM is particularly useful for imaging materials with a mixed elemental composition.

Two-dimensional (2D) materials, a structure family introduced by Novoselov and Geim exfoliating single-layer graphene from graphite,[2] provide due to their thinness ideal samples for TEM techniques, especially for atomically resolved quantification of irradiation effects.[3] This is important because the electron beam can cause changes in the structure of a specimen. Radiation damage in the TEM can be divided into knock-on damage, radiolysis, and chemical etching.[4] The exact mechanism of radiation damage in a specific material is of practical interest as it determines what options are available for minimizing it.

Ballistic displacements (so called knock-on damage) are caused by (quasi-)elastic scattering, where the electron directly transfers momentum to an atomic nucleus. If the resulting kinetic energy of the atom exceeds the displacement threshold energy (T_d), the atom is ejected from its lattice position.[5,6] When the knock-on mechanism is predominant, reducing the TEM acceleration voltage will suppress damage.[7] This process is well understood, especially in graphene,[7,8] although recent studies have suggested that dynamics at its impurity sites cannot be explained by purely elastic effects.[9,10]

Although radiolysis – the direct breaking of bonds due to the ionization of valence electrons – is assumed to be predominant in insulators, in conducting materials it is largely quenched due to rapid neutralization. In inorganic solids, both knock-on and ionization effects can take place, sometimes simultaneously. If, on the other hand, the damaging effects arise from beam heating or from electrostatic charging of an insulating specimen, reducing the incident beam current can be helpful.[11] To understand the interaction of electrons with different materials, especially semiconductors or insulators, where knock-on is not the only relevant damage mechanism, a theoretical model describing the process is needed.

For molybdenum disulfide (MoS_2), recent studies have taken the first steps toward quantitative understanding, suggesting excitation-assisted knock-on damage to be the dominant mechanism at electron energies below 80 keV.[12,13] Kretschmer et al. proposed a way to quantify both effects in a combined theoretical framework,[14] and the model was further improved by

T. A. Bui, G. T. Leuthner, J. Madsen, M. R. A. Monazam, A. I. Chirita, A. Postl, C. Mangler, J. Kotakoski, T. Susi
University of Vienna
Faculty of Physics
Boltzmanngasse 5, Vienna 1090, Austria
E-mail: thuyan.bui@univie.ac.at; toma.susi@univie.ac.at

The ORCID identification number(s) for the author(s) of this article can be found under https://doi.org/10.1002/smll.202301926

DOI: 10.1002/smll.202301926

Speckmann et al., removing the ambiguity in model parameters.[15] Additionally, Yoshimura et al. created a quantum theory of electronic excitation and sputtering and applied it to both MoS_2 and hexagonal boron nitride (hBN).[16]

However, the experimental data on hBN available until now has left much to be desired, and thus further developments urgently need accurate quantitative measurements. In particular, the residual vacuum can cause damage to the specimen due to beam-induced chemical etching.[17] The electron beam dissociates gas molecules, which can then react with atoms of the lattice. This process is responsible for the growth of pores in graphene,[18] and almost certainly also in hBN, which is how the only available quantitative data was collected.[19]

Defects in hBN are especially interesting for quantum light emission, as its color centers display bright[20] and thermally stable[21] single-photon emission across a wide spectral range.[22–24] As such, hBN has potential as a useful platform for quantum computation, information networks, and sensors.[25] Irradiation with lasers,[26] ions,[27] neutrons,[28] or electrons[29,30] have emerged as viable techniques for creating such color centers, and although their exact atomic configuration has been unclear, point defects are certainly involved.[22,30–33] However, considering the rapid damage and creation of pores under typical TEM conditions,[6,19] it has not been clear whether single vacancies can be controllably created.

2. Results and Discussion

We carried out measurements in ultra-high vacuum (UHV), which suppresses unwanted chemical etching and allows us to obtain separate cross sections for individual B and N at atomic resolution. Chemical etching occurs already at a typical residual vacuum pressure of $\approx 10^{-7}$ mbar,[17] which can even change the dominant termination of pore edges in electron-irradiated graphene.[18] Indeed, the cross sections we measure are up to three orders of magnitude lower than what was reported for atoms at pore edges,[6,19] suggesting previous experiments have been dominated by chemical etching and showing that single vacancies can indeed be created by electron irradiation at intermediate energies.

Samples were prepared using commercial hBN grown by chemical vapor deposition following the procedure of Ref. [34] (see Experimental Methods and Figure S1, Supporting Information), containing clean areas up to 100 nm in size. An overview at different length scales is provided in **Figure 1**. Exemplary STEM medium-angle annular dark-field image series recorded at an energy of 55 keV are displayed in **Figures 2** and **3**, which show both raw data, as well as double-Gaussian filtered images.[35] Each frame has 512 × 512 pixels for a field of view of typically 2 × 2 nm^2 and a scanning time of roughly 0.26 s. While scanning even faster would be beneficial, we found that this would have degraded the signal to noise ratio too much for reliable analysis.

Only cases where we could unambiguously identify the first ejected atom were included in the analysis. Cases where two separate vacancies of the same element were present in the first defected frame were counted as only a single vacancy, since the creation of the first could have facilitated the second. Just twice in all our data were two separated N and B atoms missing in the first defective frame, illustrating a high probability to create single vacancies.

To identify the number of frames without a defect and the position where the first vacancy occurred, a machine-learning algorithm based on a convolutional neural network was used to assist human analysis (see Methods and Supporting Information). The experimental displacement cross section[3,5,7,36] can be derived from the electron dose ϕ, which consist of dose rate ϕ_R multiplied by time until the defect t_d (detailed calculation can be found in the Supporting Information). It corresponds, following Poisson statistics, to the expectation value of the dose for the distribution arising from a large number of repeated measurements.

Dose rates were evaluated by estimating the beam current impinging on the sample via continuous measurement of the current falling on the virtual objective aperture of the microscope, which is saved with the image metadata. This current in turn was calibrated against the beam current measured at the drift tube of the electron energy-loss spectrometer. While typically the beam current is measured only occasionally, we recently found this may lead to significant errors in the estimated doses, and thus have used here the statistical measurements described in Ref. [15].

The displacement cross section σ describes the probability of an energetic electron scattering from an atomically thin sample to lead to a displacement of one of its atoms, calculated as the inverse of the Poisson expectation value multiplied by the material-specific areal density ρ_{hBN} (see Supporting Information for more detail). To obtain accurate values of such a stochastic process, measurements of pristine areas need to be repeated until sufficient statistics are collected. Our analysis includes 664 valid series for N and 337 for B (Figure S2, Supporting Information displays histograms of the data).

2.1. Simulation of Ionization-Assisted Displacement Thresholds

To study the role that valence ionization might play in the knock-on damage process, we performed density functional theory molecular dynamics (DFT/MD) simulations of the ejection of either N or B atoms from hBN following our established methodology[8,37] (see Methods for more detail). In addition to ground-state calculations previously reported for hBN,[6] we now use constrained DFT (cDFT) to confine a charge on the ejecting atom to quantify its effect on the displacement threshold energy. We note that this description is not entirely realistic, as the confining potential has no direct physical interpretation, and it is enforced for the full duration of the simulation (i.e. there is no charge neutralization). Accurately describing dynamics with a localized valence hole in periodic supercell is a difficult challenge, and thus this approach should be considered as a pragmatic, if imperfect approximation.

In earlier work, Kotakoski et al.[6] calculated the displacement thresholds for B and N atoms in the pristine structure and at different vacancy edges in various total charge states. For pristine structures in the ground state, they obtained $T^B_{\mathrm{gs}} = 19.36$ eV and $T^N_{\mathrm{gs}} = 23.06$ eV, somewhat different than our values of $T^B_{\mathrm{gs}} = 20.15$ eV and $T^N_{\mathrm{gs}} = 22.25$ eV. We recently noticed that the specific value of Fermi smearing used in GPAW seems to have an influence of about this magnitude on the absolute threshold energy values,[10] though also the difference between the two elements

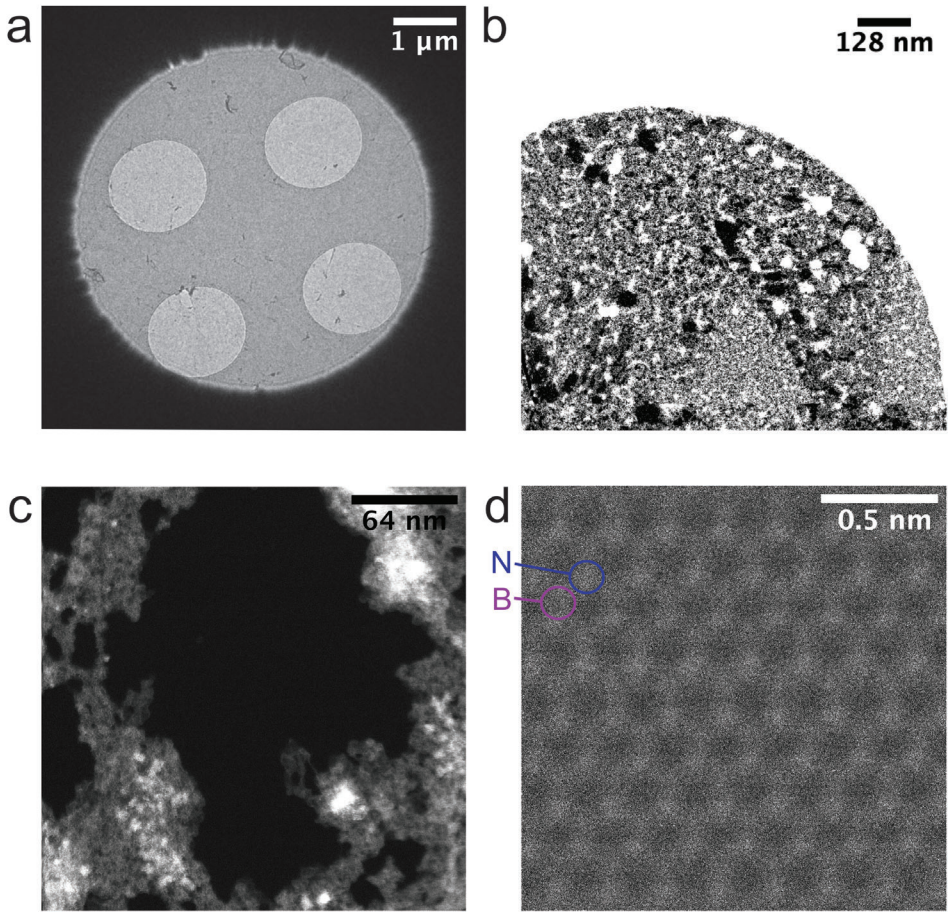

Figure 1. STEM images showing an hBN sample at different magnifications. a) Bright-field Ronchigram image of the sample support foil covered with monolayer hBN seen within the virtual objective aparture. b) MAADF image of single layer of hBN suspended over a hole. The darkest area corresponds to a clean lattice, whereas the brighter areas are covered with surface contamination. The white area surrounding the sample corresponds to the support foil. c) Area of relatively clean monolayer hBN. d) Atomic resolution MAADF image of monolayer hBN.

also seems to be slightly different (3.7 eV vs. 2.1 eV). Nonetheless, the two calculations are in general agreement.

For a full positive constrained elementary charge (corresponding to a missing electron), we find that the displacement threshold for N drops from 22.25 to 9.15 eV (−59%), while that for B drops from 20.15 to 5.05 eV (−75%). Since it is likely that even in an insulating material such as hBN, some part of the ionized charge is neutralized during the roughly 100 fs it takes for the impacted atom to fully displace, we also considered partial charges to study the systematic behavior of the threshold energy. These results are shown in **Figure 4**: after a slighter reduction for the 0.25 hole, the values drop roughly linearly with a slope of −16.3 eVe^{-1} for N and −18.2 eVe^{-1} for B.

2.2. Theoretical Cross Section with Ionization

From the displacement threshold energy T_d^{gs} one can estimate the displacement cross section σ under known electron-beam conditions using the McKinley-Feshbach formalism[38] for Coulombic scattering of relativistic electrons.[39] The corresponding total elastic displacement cross section,[36,40] with the velocities v of the atoms accounted for using phonon modeling[8] (as described in the Methods), can be written as

$$\sigma_{KO}(E_e, v) = 4\pi\left(\frac{Ze^2}{4\pi\epsilon_0 2\gamma m_0 c^2 \beta^2}\right)^2 \left\{\left(\frac{E_{max}(v)}{T_d^{gs}} - 1\right) - \beta^2 \ln\left(\frac{E_{max}(v)}{T_d^{gs}}\right) + \pi Z\alpha\beta\left[2\left(\sqrt{\frac{E_{max}(v)}{T_d^{gs}}} - 1\right) - \ln\left(\frac{E_{max}(v)}{T_d^{gs}}\right)\right]\right\} \quad (1)$$

where $E_{max}(v)$ is the maximum transferred energy at out-of-plane velocity v, Z is the atomic number, e the elementary charge, ϵ_0 the electric constant in vacuum, m_0 the electron rest mass, and α the fine-structure constant. The relativistic Lorentz factor is $\gamma = \sqrt{1-\beta^2}$ and β depends on the primary beam energy E_e as

$$\beta(E_e) = \sqrt{1 - \left(1 + \frac{E_e}{m_0 c^2}\right)^{-2}} \quad (2)$$

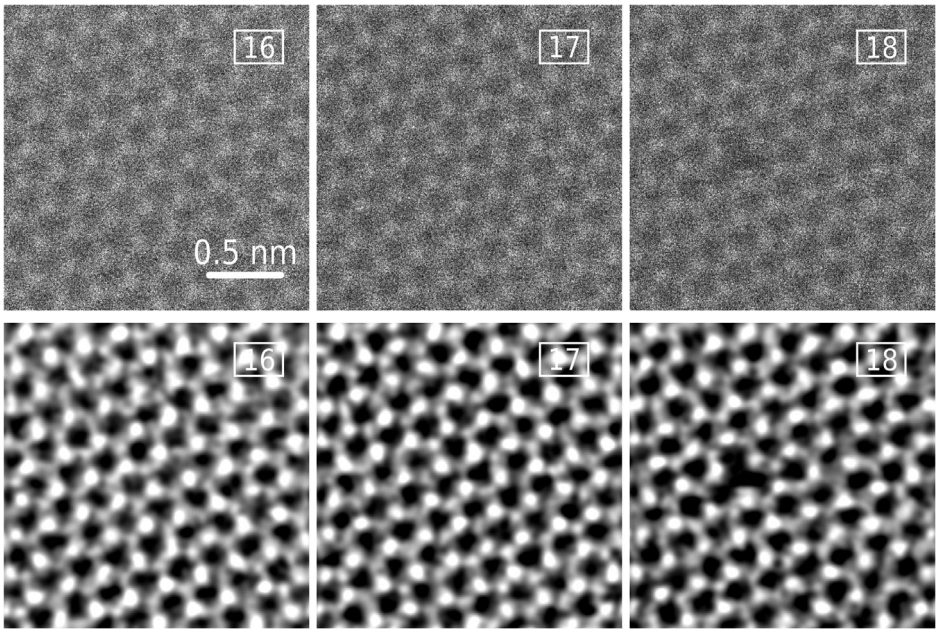

Figure 2. STEM MAADF images showing the creation of a single B vacancy. The first two unprocessed images (upper row) are from the image sequence before the defect appears. The overlaid numbers are the number of each image in the series. Image 18 shows the first B vacancy. Images in the lower row have been processed using the double-Gaussian filter ($\sigma_1 = 0.23$, $\sigma_2 = 0.15$, weight = 0.28).

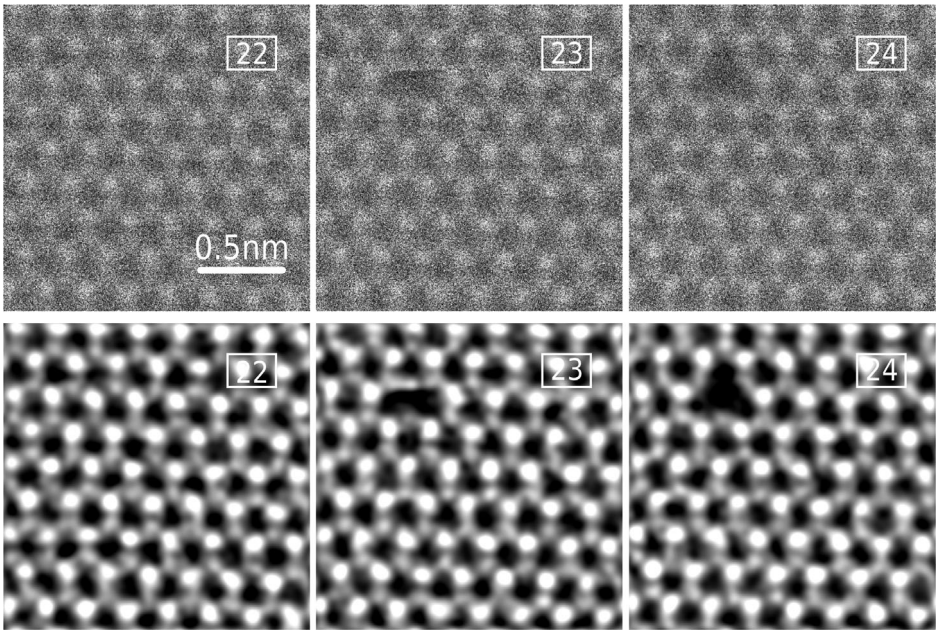

Figure 3. STEM MAADF images showing the creation of a single N vacancy. First unprocessed image (upper row) is from the image sequence before the defect appears. The overlaid numbers are the number of each image in the series. Image 23 shows where N atom ejection occurs during scanning, and image 24 shows the first N vacancy. Images in the lower row have been processed using the double Gaussian filter ($\sigma_1 = 0.24$, $\sigma_2 = 0.16$, weight = 0.29).

Previously, only the ground-state dynamics were considered. However, beam-induced excitation may reduce the bonding energy of the atoms in the lattice, thus reducing their threshold energy. While the displacement caused by an elastic scattering process (knock-on) is well understood and theoretically described, the role of inelastic electron-electron scattering still remains unclear. A classical theoretical model was derived by Bethe,[41] later on complemented relativistically by Møller.[42] A modification of Bethe's theoretical formula by using an impact parameter and substitutions to fit experiments was done by Williams,[43] which is the source of the inelastic scattering cross section reprinted in Williams & Carter.[44] However, despite being well known, that

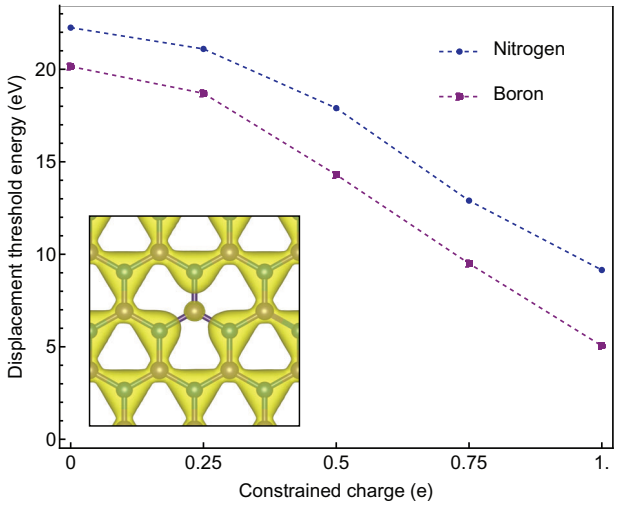

Figure 4. Reduction of the displacement threshold energy T_d as a function of charge constrained on the ejecting element. The inset shows a charge-density isosurface of a 1.0 hole constrained on the B atom at the start of a cDFT/MD simulation (isovalue 0.15 eÅ^{-3}).

formula was provided in CGS units and the definition of the included velocity term was not explicitly given. It is therefore worth reprinting it here, with some modification.

In SI units, the ionization cross section for shell s is (see Supporting Information)

$$\sigma_{\mathrm{Bethe}}(E_e, s, i) = \left(\frac{2\pi e^4 b_s n_s}{(4\pi\epsilon_0)^2 m_0 c^2 \beta^2 E_i^{\mathrm{ion}}}\right) \times\left\{\ln\left[c_s\left(\frac{m_0 c^2 \beta^2}{2E_i^{\mathrm{ion}}}\right)\right] - \ln\left(1-\beta^2\right) - \beta^2\right\} \quad (3)$$

where n_s is the number of electrons in the subshell that is ionized, b_s and c_s are a priori unknown constants for that shell, and E_i^{ion} is in our treatment the ith ionization energy. For a given electron shell and known ionization energies, cross-section data measured for atoms can be fitted to obtain the constants. As this data is available for low primary beam energies (up to 1 keV for B[45] and 5 keV for N[46]), care must be made to fit the highest-energy data points as well as possible so that the slope extending to our experimental energy range is correct (see Supporting Information for detail).

As will be discussed in the next section, it turns out that to be able to fit experimental hBN data, we needed to include two ionized states for boron (Figure S5, Supporting Information) and three for nitrogen (Figure S6, Supporting Information). The calculated ionization cross sections, extrapolated to our experimentally relevant primary beam energies, are shown in Figure S7 (Supporting Information). The cross-section values are on the order of 10^6 barn and show the characteristic $1/E$ dependence, though it should be noted that their ratio remains almost constant at 0.68–0.69 across the TEM-relevant range of energies (20–100 keV). However, as we will see when trying to describe the experimental displacement data for hBN, we had to modify the probabilities of each ionized state to obtain a good match.

2.3. Fitting Experimental Cross Sections

In hBN the mass difference between the two constituent elements is more than 20%. For nitrogen, we only need to consider the stable ^{14}N isotope. However, boron has two abundant stable isotopes with a significant relative mass difference, and thus we need to consider separately ^{10}B and ^{11}B with ca. 20 atom-% and 80 atom-% where the masses are 10.01 u and 11.01 u. Due to the greater mass of nitrogen, elastic energy transfers from primary beam electrons at our experimental energies are suppressed at displacement threshold energies below 19 eV, significantly below what DFT predicts (Figure 6), which means that the displacement of nitrogen from the ground state cannot happen at energies up to 90 keV.

Figures 5 and **6** show a fitting of the experimental data with our theoretical model that combines the earlier mentioned elastic and inelastic scattering processes (see also Supporting Information). (The experimental points at 75 keV for both elements were excluded from the fits as outliers, and we suspect that our experimental beam current at that energy does not match the measured calibrations.) The total displacement cross section σ_{tot} is calculated as a additive combination of the ground $\sigma_{\mathrm{KO}}(E_e, \nu, T_{\mathrm{d}}^{\mathrm{gs}})$ and excited

$\sigma_{\mathrm{KO}}(E_e, \nu, T_{\mathrm{d},i}^{\mathrm{ex}})$ states multiplied by the corresponding Bethe cross sections and areal density ρ_{at}:

$$\sigma_{\mathrm{tot}} = \sigma_{\mathrm{KO}}(E_e, \nu, T_{\mathrm{d}}^{\mathrm{gs}}) + \sum_{i=i_1}^{i_{\max}} \sigma_{\mathrm{KO}}(E_e, \nu, T_{\mathrm{d},i}^{\mathrm{ex}}) \cdot (\sigma_{\mathrm{Bethe}}(E_e, s, i) \cdot \xi_i) \cdot \rho_{\mathrm{at}}, \quad (4)$$

where i indexes the ionization state (up to $i_{\max} = 2$ for B and 3 for N) and ξ_i is a parameter accounting for inaccuracies in the ionization cross sections as well as finite lifetimes of the excited states. As the material consists of two elements, two separate analyses were conducted, with the earlier mentioned isotope-weighted average used for boron.

It is clear from the plots that the theoretically predicted ground-state threshold energies cannot alone describe the observed cross-section values – indeed, for nitrogen no damage would be expected up to 90 keV even if the ground-state threshold energy was as low as 19 eV – whereas the combined model does provide a good fit with the data. However, we did have to significantly increase the atomic ionization cross sections for the first ionized state: 2.92 times for boron and as much as 18.4 times for nitrogen. Only values smaller than one can be explained by a finite lifetime of the excitation.[15,16]

2.4. Discussion

We must note that the model described above is simplified in two important ways. First, the ionization energies used for the Bethe cross section in Equation 3 are tabulated for sequential ionization, i.e., the removal of further electrons from an already ionized atom, which is unlikely to be the case experimentally for hBN (and would require the multiplication of ionization probabilities). We consider the model as an approximate description of the more likely situation, namely multiple ionization by the

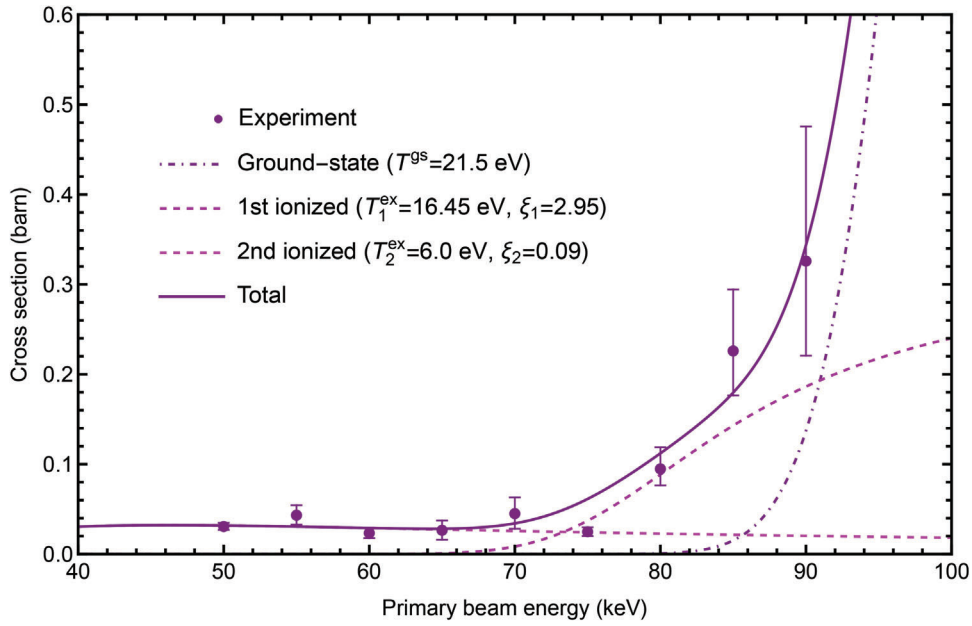

Figure 5. Displacement cross sections for boron. Theoretical fits to experimentally measured datapoints.

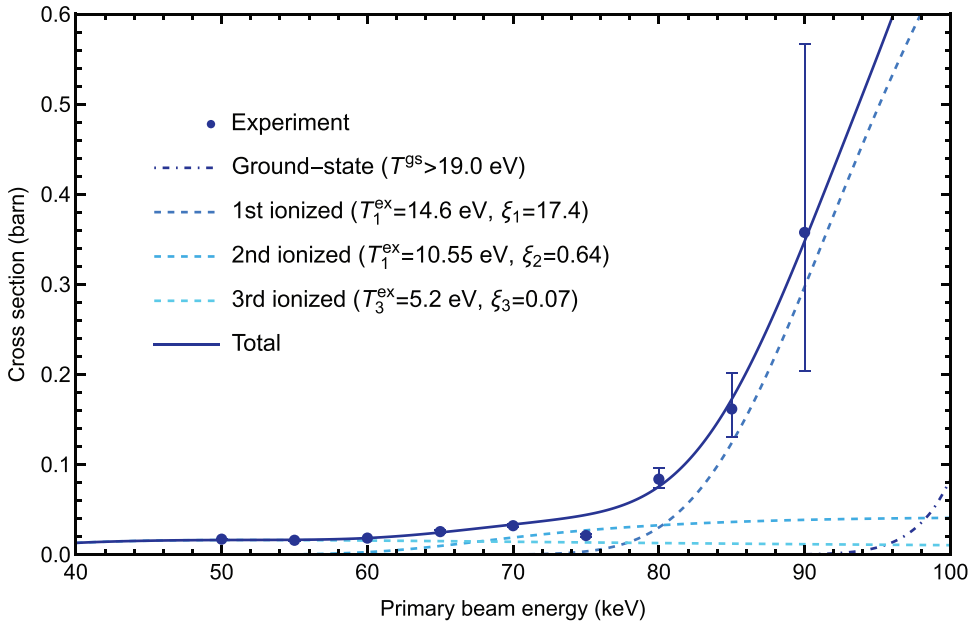

Figure 6. Displacement cross sections for nitrogen. Theoretical fits to experimentally measured datapoints.

same electron. Second, the probability of being in an ionized state should be subtracted from the ground-state process, as done in Ref. [15]. However, in our case this is not possible, as allowing ξ_1 to take values above one – indicating that the fitted atomic ionization cross sections underestimate the probability of ionization in hBN or that the process cannot correctly be described using this model – would mean that probabilities do not sum correctly. We have therefore neglected this correction, which would slightly lower the fitted ground-state threshold energies.

Using ionization cross-section data measured for atoms is clearly not ideal for describing a periodic solid with significant ionic character. Measurements on more closely related molecules, such as borazine, or even better, hexaborane, might provide an improved reference model. Even better would be direct measurements on hBN itself at the experimentally relevant TEM energies, but this is clearly not feasible using crossed beams of electrons and fast atoms or molecules that are the standard method to measure impact ionization cross sections.[47] Nonetheless, due to the relatively weak dependence of the extrapolated high-energy tail of the cross sections on the details of the fitting of the low-energy data, we agree with Kretschmer et al.[14] that this approach can provide a useful approximation.

The range of fitted excited-state thresholds falls within the simulated cDFT/MD values, but it is difficult to predict them for specific ionization states from first principles. Constrained DFT as a starting point for Ehrenfest dynamics is not feasible due to the artificial nature of the constraining potential: time-dependent dynamics without the constraint lead to rapid neutralization of the charge on a timescale much shorter than the time to displace an atom. Thus, further theory development based on the precise cross-section values reported here will be needed for a correct first-principles description of hBN irradiation damage.

A recent study has suggested that nitrogen vacancies are the active color center in hBN.[30] Our precise experimental measurements seem to indicate that it is quite challenging to exclusively create N vacancies, as the cross section for knocking out B atoms is higher across the range of studied energies. Nonetheless, even parallel-beam irradiation at 200 keV can apparently controllably create optically active regions in hBN.[30] This may be explainable by the extrapolation of our cross sections to higher primary beam energies: at 200 keV, due to its lower threshold energies and the decreased importance of their mass difference, the ejection of N becomes more likely than that of B (Figure S8, Supporting Information). This could result in a greater number of N vacancies at a fixed irradiation dose. Additional data at primary beam energies higher than 90 keV would be helpful to further reduce the related uncertainties, but the rapidly increasing damage cross section means that even at 90 keV, in many data series, larger defects appear already as the very first defect, making it impossible to assign the element to the first ejection and thus to obtain reliable estimates.

Now that it is clear that hBN is remarkably radiation resistant at primary beam energies below 80 keV, the creation of color centers could potentially be greatly optimized by site-selective irradiation using a focused STEM electron probe[48] coupled with low-dose imaging and automation enabled by machine learning.[49]

3. Conclusion

Despite its insulating nature, monolayer hexagonal boron nitride is surprisingly stable under electron irradiation when chemical etching can be prevented. Single boron and nitrogen vacancies can be created at intermediate electron energies, although boron is twice as likely to be ejected due to its lower mass. However, we predict that at energies of 200 keV and above, crnitrogen in turn becomes easier to eject. Providing reliable experimental measurements to develop theoretical models can lead to a better understanding of ionization damage in non-conducting materials more broadly, where a combination of inelastic and elastic scattering appears to be active. Further, point defects in hBN are of great current interest due to their single-photon emission properties, and it may be possible to use electron irradiation to purposefully create them. New opportunities for atomically precise manipulation, until now demonstrated for dopant atoms in graphene and in bulk silicon, may also be uncovered.

4. Experimental Section

Sample Preparation: Commercial monolayer hBN synthesized with chemical vapor deposition[50] purchased from Graphene Supermarket (CVD hBN on copper foil) was transferred onto a conventional Au Quantifoil TEM grid (R 1.2/1.3) (Figure S1a, Supporting Information). To attach the TEM grids onto hBN, a drop of isopropanol (IPA) was put on top of the already placed grid (Figure S1b, Supporting Information). For a successful transfer, uniform adhesion between the substrate and the TEM grids was necessary. To etch away the copper foil, this study used an 10% iron(III)-chloride ($FeCl_3$) acid solution (Figure S1c, Supporting Information). The sample was introduced to vacuum and baked overnight at ca. 150 °C before measurements were conducted. Between measurements, the sample was stored in the CANVAS ultra-high vacuum system.[51]

Scanning Transmission Electron Microscopy and Analysis: STEM measurements were performed with an aberration-corrected Nion UltraSTEM100 at primary beam energies ranging from 50 to 90 keV. Image series were recorded using a medium-angle annular dark field (MAADF) detector with a collection angle of 80–200 mrad. The base pressure at the sample was below 10^{-9} mbar, suppressing any chemical etching.[17]

A machine-learning algorithm based on a convolutional neural network trained using simulated images[52] was used to detect the position of the first occurring defect in each recorded image series. The intensity difference between the N and B sublattices was also used to determine which element was ejected, and the analysis results were verified by manual inspection (see Supporting Information for detail).

Density Functional Theory Molecular Dynamics: To perform the simulations, this study used the Atomic Simulation Environment[53] for Velocity-Verlet dynamics with a timestep of 0.3 fs on a $7 \times 7 \times 1$ graphene supercell, with forces from a GPAW[54] calculator with the PBE functional,[55] a localized *dzp* basis set, a $5 \times 5\times 1$ Monkhorst-Pack **k**-point grid, and a Fermi-Dirac smearing of 0.025 eV.

The GPAW implementation of cDFT imposed a localized constraining potential via an atom-centered Gaussian function,[56] whose weight is iteratively optimized to achieve the desired charge on the atom as assessed by Hirshfeld partitioning.[57] For the ground state, this study considered both spin-paired and spin-polarized calculations, whereas the charge-constraint was always imposed on one spin channel. Also simulated were $6 \times 6 \times 1$ and $5 \times 5 \times 1$ supercells, which confirmed that the calculated threshold energies were converged within 0.1 eV.

Phonon Density of States: Phonon calculations were performed using density functional perturbation theory (DFPT)[58,59] as implemented in the ABINIT code.[60] The lattice structure was first optimized down to an energy difference of 10^{-10} Ha with a **k**-point mesh of $20 \times 20 \times 1$ and an energy cut-off of 55 Ha. Exchange and correlation were described using the local density approximation and the Troullier–Martins norm-conserving pseudo-potential.[61]

For calculating the Hessian and dynamical matrix, the ground-state wave functions were converged to within 10^{-18} Ha^2 with a **k**-point mesh of $40 \times 40 \times 1$. Phonon density of states (DOS) was interpolated using the Gaussian method with a smearing of 6.5×10^{-5} Ha, and assigned to the B and N sublattice to estimate their out-of-plane mean-square velocities as described in Ref. [8]. The calculated phonon DOS is shown as Figure S9 (Supporting Information) and included in numerical form as Supporting File.

Supporting Information

Supporting Information is available from the Wiley Online Library or from the author.

Acknowledgements

T.A.B, J.M., M.R.A.M., A.I.C., A.P., and T.S. were supported by the European Research Council (ERC) under the European Union's Horizon 2020 research and innovation programme (Grant agreement no. 756277-ATMEN). The authors gratefully acknowledge computational resources provided by the Vienna Scientific Cluster (VSC).

Conflict of Interest

The authors declare no conflict of interest.

Data Availability Statement

The raw experimental STEM data that support the findings of this study are openly available in PHAIDRA at https://doi.org/10.25365/phaidra.399, reference number 1649515.

Calculations and fitting of the theoretical cross section models to the data (Wolfram Mathematica 13.1 notebook) can be accessed on the Wolfram Notebook Archive at https://notebookarchive.org/2023-05-4lw178w.

Keywords

hexagonal boron nitride, scanning transmission electron microscopy, ultra-high vacuum

Received: March 6, 2023
Revised: May 16, 2023
Published online: June 1, 2023

[1] A. V. Crewe, *Science* **1966**, *154*, 729.
[2] K. S. Novoselov, A. K. Geim, S. V. Morozov, D. Jiang, Y. Zhang, S. V. Dubonos, I. V. Grigorieva, A. A. Firsov, *Science* **2004**, *306*, 666.
[3] T. Susi, J. C. Meyer, J. Kotakoski, *Nat. Rev. Phys.* **2019**, *1*, 397.
[4] R. Egerton, P. Li, M. Malac, *Micron* **2004**, *35*, 399.
[5] F. Banhart, *Rep. Prog. Phys.* **1999**, *62*, 1181.
[6] J. Kotakoski, C. H. Jin, O. Lehtinen, K. Suenaga, A. V. Krasheninnikov, *Phys. Rev. B* **2010**, *82*, 113404.
[7] J. C. Meyer, F. Eder, S. Kurasch, V. Skakalova, J. Kotakoski, H. J. Park, S. Roth, A. Chuvilin, S. Eyhusen, G. Benner, A. V. Krasheninnikov, U. Kaiser, *Phys. Rev. Lett.* **2012**, *108*, 196102.
[8] T. Susi, C. Hofer, G. Argentero, G. T. Leuthner, T. J. Pennycook, C. Mangler, J. C. Meyer, J. Kotakoski, *Nat. Commun.* **2016**, *7*, 13040.
[9] T. Susi, D. Kepaptsoglou, Y.-C. Lin, Q. M. Ramasse, J. C. Meyer, K. Suenaga, J. Kotakoski, *2D Mater.* **2017**, *4*, 042004.
[10] A. Chirita, A. Markevich, M. Tripathi, N. A. Pike, M. J. Verstraete, J. Kotakoski, T. Susi, *Phys. Rev. B* **2022**, *105*, 235419.
[11] R. Egerton, *Microsc. Res. Tech.* **2012**, *75*, 1550.
[12] R. Zan, Q. M. Ramasse, R. Jalil, T. Georgiou, U. Bangert, K. S. Novoselov, *ACS Nano* **2013**, *7*, 10167.
[13] G. Algara-Siller, S. Kurasch, M. Sedighi, O. Lehtinen, U. Kaiser, *Appl. Phys. Lett.* **2013**, *103*, 203107.
[14] S. Kretschmer, T. Lehnert, U. Kaiser, A. V. Krasheninnikov, *Nano Lett.* **2020**, *20*, 2865.
[15] C. Speckmann, J. Lang, J. Madsen, M. R. A. Monazam, G. Zagler, G. T. Leuthner, N. McEvoy, C. Mangler, T. Susi, J. Kotakoski, *Phys. Rev. B* **2023**, *107*, 094112.
[16] A. Yoshimura, M. Lamparski, J. Giedt, D. Lingerfelt, J. Jakowski, P. Ganesh, T. Yu, B. G. Sumpter, V. Meunier, *Nanoscale* **2022**, *15*, 1053.
[17] G. T. Leuthner, S. Hummel, C. Mangler, T. J. Pennycook, T. Susi, J. C. Meyer, J. Kotakoski, *Ultramicroscopy* **2019**, *203*, 76.
[18] G. T. Leuthner, T. Susi, C. Mangler, J. C. Meyer, J. Kotakoski, *2D Mater.* **2021**, *8*, 035023.
[19] O. Cretu, Y.-C. Lin, K. Suenaga, *Micron* **2015**, *72*, 21.
[20] T. T. Tran, K. Bray, M. J. Ford, M. Toth, I. Aharonovich, *Nat. Nanotechnol.* **2016**, *11*, 37.
[21] M. Kianinia, B. Regan, S. A. Tawfik, T. T. Tran, M. J. Ford, I. Aharonovich, M. Toth, *ACS Photonics* **2017**, *4*, 768.
[22] T. T. Tran, C. Elbadawi, D. Totonjian, C. J. Lobo, G. Grosso, H. Moon, D. R. Englund, M. J. Ford, I. Aharonovich, M. Toth, *ACS Nano* **2016**, *10*, 7331.
[23] R. Bourrellier, S. Meuret, A. Tararan, O. Stéphan, M. Kociak, L. H. G. Tizei, A. Zobelli, *Nano Lett.* **2016**, *16*, 4317.
[24] A. Gottscholl, M. Kianinia, V. Soltamov, S. Orlinskii, G. Mamin, C. Bradac, C. Kasper, K. Krambrock, A. Sperlich, M. Toth, I. Aharonovich, V. Dyakonov, *Nat. Mater.* **2020**, *19*, 540.
[25] N. P. de Leon, K. M. Itoh, D. Kim, K. K. Mehta, T. E. Northup, H. Paik, B. S. Palmer, N. Samarth, S. Sangtawesin, D. W. Steuerman, *Science* **2021**, *372*, eabb2823.
[26] L. Gan, D. Zhang, R. Zhang, Q. Zhang, H. Sun, Y. Li, C.-Z. Ning, *ACS Nano* **2022**, *16*, 14254.
[27] S. Choi, T. T. Tran, C. Elbadawi, C. Lobo, X. Wang, S. Juodkazis, G. Seniutinas, M. Toth, I. Aharonovich, *ACS Appl. Mater. Interfaces* **2016**, *8*, 29642.
[28] H. Zhang, M. Lan, G. Tang, F. Chen, Z. Shu, F. Chen, M. Li, *J. Mater. Chem. C* **2019**, *7*, 12211.
[29] A. L. Exarhos, D. A. Hopper, R. R. Grote, A. Alkauskas, L. C. Bassett, *ACS Nano* **2017**, *11*, 3328.
[30] C. Su, F. Zhang, S. Kahn, B. Shevitski, J. Jiang, C. Dai, A. Ungar, J.-H. Park, K. Watanabe, T. Taniguchi, J. Kong, Z. Tang, W. Zhang, F. Wang, M. Crommie, S. G. Louie, S. Aloni, A. Zettl, *Nat. Mater.* **2022**, *21*, 896.
[31] D. Wong, J. Velasco, L. Ju, J. Lee, S. Kahn, H.-Z. Tsai, C. Germany, T. Taniguchi, K. Watanabe, A. Zettl, F. Wang, M. F. Crommie, *Nat. Nanotechnol.* **2015**, *10*, 949.
[32] M. Abdi, J.-P. Chou, A. Gali, M. B. Plenio, *ACS Photonics* **2018**, *5*, 1967.
[33] H. Schauffert, J. C. Stewart, S. Ali, S. Walser, H. Hörner, A. S. Prasad, V. Babenko, Y. Fan, D. Eder, K. S. Thygesen, S. Hofmann, B. C. Bayer, S. M. Skoff, Quantum Physics **2023**, arXiv:2210.11099 [quant-ph].
[34] M. R. Ahmadpour Monazam, U. Ludacka, H.-P. Komsa, J. Kotakoski, *Appl. Phys. Lett.* **2019**, *115*, 071604.
[35] O. L. Krivanek, M. F. Chisholm, V. Nicolosi, T. J. Pennycook, G. J. Corbin, N. Dellby, M. F. Murfitt, C. S. Own, Z. S. Szilagyi, M. P. Oxley, S. T. Pantelides, S. J. Pennycook, *Nature* **2010**, *464*, 571.
[36] A. Zobelli, A. Gloter, C. P. Ewels, G. Seifert, C. Colliex, *Phys. Rev. B* **2007**, *75*, 245402.
[37] T. Susi, J. Kotakoski, R. Arenal, S. Kurasch, H. Jiang, V. Skakalova, O. Stephan, A. V. Krasheninnikov, E. I. Kauppinen, U. Kaiser, J. C. Meyer, *ACS Nano* **2012**, *6*, 8837.
[38] W. A. McKinley, H. Feshbach, *Phys. Rev.* **1948**, *74*, 1759.
[39] C. Su, M. Tripathi, Q.-B. Yan, Z. Wang, Z. Zhang, C. Hofer, H. Wang, L. Basile, G. Su, M. Dong, J. C. Meyer, J. Kotakoski, J. Kong, J.-C. Idrobo, T. Susi, J. Li, *Sci. Adv.* **2019**, *5*, eaav2252.
[40] R. Dugdale, A. Green, *The London, Edinburgh, and Dublin Philosophical Magazine and Journal of Science* **1954**, *45*, 163.
[41] H. Bethe, *Ann. Phys.* **1930**, *397*, 325.
[42] C. Møller, *Ann. Phys.* **1932**, *406*, 531.
[43] E. Williams, *Proceedings of the Royal Society of London. Series A, Containing Papers of a Mathematical and Physical Character* **1933**, *139*, 163.
[44] D. B. Williams, C. B. Carter, *Transmission electron microscopy: a textbook for materials science*, 2nd ed edition, Springer, New York **2009**.
[45] Y.-K. Kim, P. M. Stone, *Phys. Rev. A* **2001**, *64*, 052707.
[46] Y.-K. Kim, J.-P. Desclaux, *Phys. Rev. A* **2002**, *66*, 012708.
[47] E. Brook, M. F. A. Harrison, A. C. H. Smith, *Journal of Physics B: Atomic and Molecular Physics* **1978**, *11*, 3115.
[48] T. Susi, J. Meyer, J. Kotakoski, *Ultramicroscopy* **2017**, *180*, 163.
[49] K. M. Roccapriore, M. G. Boebinger, O. Dyck, A. Ghosh, R. R. Unocic, S. V. Kalinin, M. Ziatdinov, *ACS Nano* **2022**.
[50] K. K. Kim, A. Hsu, X. Jia, S. M. Kim, Y. Shi, M. Dresselhaus, T. Palacios, J. Kong, *ACS Nano* **2012**, *6*, 8583.
[51] C. Mangler, J. Meyer, A. Mittelberger, K. Mustonen, T. Susi, J. Kotakoski, *Microsc. Microanal.* **2022**, *28*, 2940.

[52] A. Trentino, J. Madsen, A. Mittelberger, C. Mangler, T. Susi, K. Mustonen, J. Kotakoski, *Nano Lett.* **2021**, *21*, 5179.
[53] A. H. Larsen, J. J. Mortensen, J. Blomqvist, I. E. Castelli, R. Christensen, M. Dułak, J. Friis, M. N. Groves, B. Hammer, C. Hargus, E. D. Hermes, P. C. Jennings, P. B. Jensen, J. Kermode, J. R. Kitchin, E. L. Kolsbjerg, J. Kubal, K. Kaasbjerg, S. Lysgaard, J. B. Maronsson, T. Maxson, T. Olsen, L. Pastewka, A. Peterson, C. Rostgaard, J. Schiøtz, O. Schütt, M. Strange, K. S. Thygesen, T. Vegge, et al., *J. Phys.: Condens. Matter* **2017**, *29*, 273002.
[54] J. Enkovaara, C. Rostgaard, J. J. Mortensen, J. Chen, M. Dulak, L. Ferrighi, J. Gavnholt, C. Glinsvad, V. Haikola, H. A. Hansen, H. H. Kristoffersen, M. Kuisma, A. H. Larsen, L. Lehtovaara, M. Ljungberg, O. Lopez-Acevedo, P. G. Moses, J. Ojanen, T. Olsen, V. Petzold, N. A. Romero, J. Stausholm-Møller, M. Strange, G. A. Tritsaris, M. Vanin, M. Walter, B. Hammer, H. Hä kkinen, G. K. H. Madsen, R. M. Nieminen, et al., *J. Phys.: Condens. Matter* **2010**, *22*, 253202.
[55] J. P. Perdew, K. Burke, M. Ernzerhof, *Phys. Rev. Lett.* **1996**, *77*, 3865.
[56] M. Melander, E. Jónsson, J. J. Mortensen, T. Vegge, J. M. García Lastra, *J. Chem. Theory Comput.* **2016**, *12*, 5367.
[57] F. L. Hirshfeld, *Theoretica Chimica Acta* **1977**, *44*, 129.
[58] S. Baroni, S. de Gironcoli, A. Dal Corso, P. Giannozzi, *Rev. Mod. Phys.* **2001**, *73*, 515.
[59] X. Gonze, C. Lee, *Phys. Rev. B* **1997**, *55*, 10355.
[60] X. Gonze, B. Amadon, P.-M. Anglade, J.-M. Beuken, F. Bottin, P. Boulanger, F. Bruneval, D. Caliste, R. Caracas, M. Côté, T. Deutsch, L. Genovese, P. Ghosez, M. Giantomassi, S. Goedecker, D. Hamann, P. Hermet, F. Jollet, G. Jomard, S. Leroux, M. Mancini, S. Mazevet, M. Oliveira, G. Onida, Y. Pouillon, T. Rangel, G.-M. Rignanese, D. Sangalli, R. Shaltaf, M. Torrent, et al., *Comput. Phys. Commun.* **2009**, *180*, 2582.
[61] N. Troullier, J. L. Martins, *Phys. Rev. B* **1991**, *43*, 8861.